

Supplementary information

Modular chiral origami metamaterials

In the format provided by the
authors and unedited

Supplementary information for Modular chiral origami metamaterials

Tuo Zhao ^{*1}, Xiangxin Dang ^{*1}, Konstantinos Manos², Shixi Zang¹, Jyotirmoy Mandal^{1,3},
Minjie Chen^{2,4}, and Glaucio H. Paulino ^{†1,3}

¹Department of Civil and Environmental Engineering, Princeton University, Princeton, NJ 08544, USA

²Department of Electrical and Computer Engineering, Princeton University, Princeton, NJ 08544, USA

³Princeton Materials Institute (PMI), Princeton University, Princeton, NJ 08544, USA

⁴Andlinger Center for Energy and the Environment, Princeton University, Princeton, NJ 08544, USA

Contents

S1	Modular cell geometry	2
S2	Chiral modular assembly geometry and kinematics	2
S3	Metamaterial scalability associated with chirality	2
S4	Experimental setups for linear displacement with free-rotation	3
S5	Theory and simulation: Bar-and-hinge model	3
S6	Magnetically actuated robotic metamaterials	6
S7	On thermoregulation of buildings	6
S8	Preisach model of the modular dipoles	7
S9	Inverse layout design for the modular cell	7
S10	Preferred modular cell design features	8
S11	Captions of supplementary videos	9

List of Figures

S1	10
S2	11
S3	12
S4	13
S5	14
S6	15
S7	16
S8	17
S9	18
S10	19
S11	20
S12	21
S13	22
S14	23
S15	24
S16	25
S17	26
S18	27

List of Tables

S1	6
----	-------	---

*These authors contributed equally to this work.

†gpaulino@princeton.edu

S1 Modular cell geometry

We consider the Kresling modular cell of n -gon bases as shown in Fig. S1. We denote the edge length of the polygon by a . Then, the radius r of the circumscribed circle of the polygon can be calculated by

$$r = \frac{a}{2 \sin(\pi/n)}. \quad (\text{S1})$$

We describe the deformation of the modular cell by two independent variables – the height h and twist angle φ . We denote the deformed rod lengths by \tilde{b} for the mountain rods and $\tilde{c}(h, \varphi)$ for the valley rods. From Ref. [S1], we know that

$$\begin{aligned} \tilde{b}(h, \varphi) &= \sqrt{h^2 + 2r^2(1 - \cos \varphi)}, \\ \tilde{c}(h, \varphi) &= \sqrt{h^2 + 2r^2[1 - \cos(\varphi + 2\pi/n)]}. \end{aligned} \quad (\text{S2})$$

We focus on the Kresling geometry with two stable configurations. For the first configuration, the height is denoted by h_1 and the twist angle is denoted by φ_1 . For the second configuration, the height is denoted by h_0 and the twist angle is denoted by φ_0 . We assume $h_1 > h_0$ so that the first configuration is unfolded, and consequently, we have $\varphi_1 < \varphi_0$. At the two stable states, the rod lengths are the same, which can be expressed as

$$\tilde{b}(h_1, \varphi_1) = b, \quad \tilde{b}(h_0, \varphi_0) = b, \quad \tilde{c}(h_1, \varphi_1) = c, \quad \tilde{c}(h_0, \varphi_0) = c. \quad (\text{S3})$$

Combining Eqs. (S2) and (S3), we obtain

$$\varphi_1 = \arccos\left(\frac{h_1^2 - h_0^2}{4r^2} \sec \frac{\pi}{n}\right) - \frac{\pi}{n}, \quad \varphi_0 = \pi - \frac{2\pi}{n} - \varphi_1. \quad (\text{S4})$$

S2 Chiral modular assembly geometry and kinematics

We aim to characterize the overall geometry of the chiral assembly. As shown in Fig. S2a, the geometry is determined by the side length \tilde{L} of the circumscribed square of the rotating-square tessellation, and the height \tilde{H} of the assembly. We denote the initial values of \tilde{L} and \tilde{H} by L and H , respectively. We can calculate \tilde{L} by

$$\tilde{L} = L \cos(\varphi/2), \quad (\text{S5})$$

in which φ is the total twist angle of a column. We define the side length ratio α and the height ratio β by

$$\alpha = \tilde{L}/L = \cos(\varphi/2) \quad \text{and} \quad \beta = \tilde{H}/H, \quad (\text{S6})$$

respectively. We can calculate the initial volume of the assembly by

$$V = L^2 H. \quad (\text{S7})$$

In a deformed state, the volume of the assembly is calculated by

$$\tilde{V} = (\alpha L)^2 \beta H. \quad (\text{S8})$$

We define the volume ratio γ by

$$\gamma = \tilde{V}/V = \alpha^2 \beta = \beta \cos^2(\varphi/2). \quad (\text{S9})$$

From a kinematics perspective, Figs. S2b and S2c demonstrate details of the rotations of the tessellations on top and bottom, respectively. For the top tessellation (Fig. S2b), the blue squares labeled with red arrows rotate, while the blue squares labeled with green arrays transform in rigid motion. For the bottom tessellation (Fig. S2c), the yellow squares labeled with green arrows rotate, while the four squares labeled with red arrow at the corners transform in rigid motion. For comparison, Fig. S2d shows the deformation of a standard rotating-square tessellation.

S3 Metamaterial scalability associated with chirality

We study the scalability of the chiral metamaterial by means of increasing the number of modular cells while fixing outer dimensions (Fig. S3). The chirality of each unit cell is associated with indices i, j, k defined in Eq. (1) in the Main Text. The desired chirality enables the assembly to achieve the least-volume configuration under a single-degree-of-freedom actuation, i.e., linear displacement with free-rotation or rotation with free-translation. To achieve the desired deformation, a linear actuator can be applied to assemblies with any number of layers. In contrast, actuation with a rotational actuator needs to impose an additional constraint, i.e., folded cells cannot be deployed for assemblies of more than four layers. Under this assumption, we conduct the analytical kinematics analysis to verify the multimodal deformation mechanisms of the assemblies with increasing system sizes. We observe distinct end configurations for the assemblies with an even number of layers and those with an odd number of layers. The deformed configurations in Figs. S3a and S3c shrink in height, while the end configurations in Figs. S3b and S3d contract in both vertical and horizontal directions. Those distinct deformed configurations enrich the deformation modality, and they can be used for applications such as robotic transformers with multi-configurations.

S4 Experimental setups for linear displacement with free-rotation

Three alternative boundary conditions are illustrated by Extended Data Fig. 2c. The first two are discussed below (Extended Data Figs. 2c-left and 2c-middle) while the third one (Extended Data Fig. 2c-right) is explained in detail in the Main Text – see Fig. 3. In addition, we further explore the third boundary condition to study a functionally graded assembly, as illustrated by Fig. S7.

Boundary Condition #1 (BC#1): The applied top boundary condition consists of a concentrated load at the center of the rotating squares (Extended Data Fig. 2c-left), and it prescribes displacement and zero out-of-plane rotation at the central squares. The bottom boundary condition consists of a fixed central portion of the rotating squares. The experimental results are summarized in Fig. S5. The camera recordings of the tests capturing the three representative configurations (Fig. S5a) show the multimodal deformation of the assembly. From state (1) to state (2), the assembly shrinks in the axial direction and twists clockwise up to 50.8° . From state (2) to (3), the assembly keeps shrinking but rotates in the counterclockwise direction. From state (3) to (4), the twisting direction of the assembly changes to the clockwise direction, and the end twist angle is 66.2° . Moreover, notice the significant out-of-plane deformation of both the top and bottom rotating-square tessellations. The experimental data provides both the mechanical behavior and kinematic behavior of the metamaterial. For instance, the force-displacement profiles (Fig. S5b) demonstrate the loading capacity of the assembly during deformation. In addition, the plots in Fig. S5c measure both the in-plane deformation (edge contraction) and the out-of-plane deformation (height shrinkage) with respect to the twist angle.

Boundary Condition #2 (BC#2): The applied top boundary condition consists of a concentrated load at the center of the rotating squares. The bottom boundary condition consists of a fixed central portion of the rotating square while preventing out-of-plane deformations and allowing free in-plane deformations by means of micro rollers with ball transfers (Extended Data Fig. 2c-middle). The experimental results are summarized in Fig. S6. Fig. S6a shows four representative configurations. Notice the significant out-of-plane deformation of the top rotating-square tessellation. Figs. S6b and S6c provide the loading capacity and the deformation of the assembly, respectively. Conceptually, this setup is an intermediate configuration with respect to the other two boundary conditions, i.e., Extended Data Fig. 2c (left) and Extended Data Fig. 2c (right).

Functionally graded cells. Furthermore, we investigate the deformation of an assembly composed of functionally graded unit cells (Fig. S7). Among the cells with different colors, red cells have the lowest energy barrier, yellow cells have the highest energy barrier, and white cells are in between. Fig. S7a shows three representative configurations of the test. From state (1) to state (2), the assembly shrinks in the axial direction as well as twists 59.3° in the clockwise direction. From state (2) to (3), the assembly keeps shrinking while the change of twist angle is less than 10° . Figs. S7b and S7c provide the loading capacity and the deformation of the assembly, respectively.

S5 Theory and simulation: Bar-and-hinge model

Unit cell. We have assumed that the unit cell has the strain energy U_{cell} given in Eq. (4) in the Methods. The total potential energy is

$$\Pi_{\text{cell}}(h, \varphi) = U_{\text{cell}}(h, \varphi) - Fh - T\varphi. \quad (\text{S10})$$

The principle of minimum potential energy reads

$$\frac{\partial U_{\text{cell}}(h, \varphi)}{\partial h} = F, \quad \frac{\partial U_{\text{cell}}(h, \varphi)}{\partial \varphi} = T. \quad (\text{S11})$$

Then, we can simulate the compression with free-rotation of a unit cell ($h = \bar{h}$, $T = 0$) by solving the following optimization problem

$$\min_{\varphi} U_{\text{cell}}(\bar{h}, \varphi) \quad \text{s.t.} \quad -(\pi - 2\pi/n) < \varphi < \pi - 2\pi/n. \quad (\text{S12})$$

The bounds of the twist angle φ are assigned to avoid contact of the members in the unit cell. Also, we can simulate the twist with free-translation of a unit cell ($\varphi = \bar{\varphi}$, $F = 0$) by solving the following optimization problem

$$\min_h U_{\text{cell}}(h, \bar{\varphi}) \quad \text{s.t.} \quad h > 0. \quad (\text{S13})$$

Column. The strain energy of a column can be obtained by simply adding up the energy of each unit cell:

$$U_{\text{column}}(h, \varphi) = \sum_k U_{\text{cell},k} [h_k(h, \varphi), \varphi_k(h, \varphi)]. \quad (\text{S14})$$

Total potential energy is

$$\Pi_{\text{column}}(h, \varphi) = U_{\text{column}}(h, \varphi) - Fh - T\varphi. \quad (\text{S15})$$

The principle of minimum potential energy reads

$$\frac{\partial U_{\text{column}}(h, \varphi)}{\partial h} = F, \quad \frac{\partial U_{\text{column}}(h, \varphi)}{\partial \varphi} = T. \quad (\text{S16})$$

Then, we can simulate the compression with free-rotation of a column ($h = \bar{h}$, $T = 0$) by solving the following optimization problem

$$\min_{h_k, \varphi_k} U_{\text{column}} \quad \text{s.t.} \quad \begin{cases} -(\pi - 2\pi/n) < \varphi_k < \pi - 2\pi/n, \quad h_k > 0, \\ \sum_k h_k = \bar{h}, \\ \frac{\partial U_{\text{cell},k}(h_k, \varphi_k)}{\partial h_k} = \frac{\partial U_{\text{cell},k+1}(h_{k+1}, \varphi_{k+1})}{\partial h_{k+1}}, \\ \frac{\partial U_{\text{cell},k}(h_k, \varphi_k)}{\partial \varphi_k} = \frac{\partial U_{\text{cell},k+1}(h_{k+1}, \varphi_{k+1})}{\partial \varphi_{k+1}}. \end{cases} \quad (\text{S17})$$

Also, we can simulate the twist with free-translation of a column ($\varphi = \bar{\varphi}$, $F = 0$) by solving the following optimization problem

$$\min_{h_k, \varphi_k} U_{\text{column}} \quad \text{s.t.} \quad \begin{cases} -(\pi - 2\pi/n) < \varphi_k < \pi - 2\pi/n, \quad h_k > 0, \\ \sum_k \varphi_k c_k = \bar{\varphi}, \\ \frac{\partial U_{\text{cell},k}(h_k, \varphi_k)}{\partial h_k} = \frac{\partial U_{\text{cell},k+1}(h_{k+1}, \varphi_{k+1})}{\partial h_{k+1}}, \\ \frac{\partial U_{\text{cell},k}(h_k, \varphi_k)}{\partial \varphi_k} = \frac{\partial U_{\text{cell},k+1}(h_{k+1}, \varphi_{k+1})}{\partial \varphi_{k+1}}. \end{cases} \quad (\text{S18})$$

The bivalued parameter c_k prescribes the chirality of the k -th unit cell, with +1 representing the chirality illustrated in Fig. S1, and -1 the opposite chirality. We have stipulated that the two representative twist angles φ_1 and φ_0 are positive, and when the unit cell is folded, the twist angle increases (i.e., $\varphi_0 > \varphi_1$, see φ_0 and φ_1 in Fig. S1).

Assembly of columns and rotating-square tessellations. We have assumed that the rotating-square tessellation has rotational stiffness k_{RS} . Confined by the top and bottom tessellations, all the columns should have the same height h and twist angle φ (subject to the opposite direction of rotation) throughout the deformation. Therefore, the strain energy of an assembly with rotating-square tessellations is

$$U_{\text{assembly}}(h, \varphi) = \sum_{k'} U_{\text{column},k'}(h, \varphi) + \frac{k_{\text{RS}}}{2} \varphi^2. \quad (\text{S19})$$

The total potential energy is

$$\Pi_{\text{assembly}}(h, \varphi) = U_{\text{assembly}}(h, \varphi) - Fh - T\varphi. \quad (\text{S20})$$

The principle of minimum potential energy reads

$$\frac{\partial U_{\text{assembly}}(h, \varphi)}{\partial h} = F, \quad \frac{\partial U_{\text{assembly}}(h, \varphi)}{\partial \varphi} = T. \quad (\text{S21})$$

Then, we can simulate the compression with free-rotation of an assembly ($h = \bar{h}$, $T = 0$) by solving the following optimization problem

$$\min_{h_{k,k'}, \varphi_{k,k'}} U_{\text{assembly}} \quad \text{s.t.} \quad \begin{cases} -(\pi - 2\pi/n) < \varphi_{k,k'} < \pi - 2\pi/n, \quad h_{k,k'} > 0, \\ \sum_k h_{k,k'} = \bar{h}, \\ r_{k'} \sum_k \varphi_{k,k'} c_{k,k'} = r_{k'+1} \sum_k \varphi_{k,k'+1} c_{k,k'+1}, \\ \frac{\partial U_{\text{cell},k,k'}(h_{k,k'}, \varphi_{k,k'})}{\partial h_{k,k'}} = \frac{\partial U_{\text{cell},k+1,k'}(h_{k+1,k'}, \varphi_{k+1,k'})}{\partial h_{k+1,k'}}, \\ \frac{\partial U_{\text{cell},k,k'}(h_{k,k'}, \varphi_{k,k'})}{\partial \varphi_{k,k'}} = \frac{\partial U_{\text{cell},k+1,k'}(h_{k+1,k'}, \varphi_{k+1,k'})}{\partial \varphi_{k+1,k'}}. \end{cases} \quad (\text{S22})$$

The bivalued parameter $c_{k,k'}$ prescribes the chirality of the k -th unit cell in the k' -th column. The bivalued parameter $r_{k'}$ represents different motions of the squares in the tessellations. As shown in Fig. S2b, for the squares that rotate,

we can set $r_{k'} = -1$ for the corresponding column; for the squares that only translate without rotation, we can set $r_{k'} = +1$ for the corresponding column. It is noteworthy that if the square in the top (bottom) tessellation does not rotate, the corresponding square in the bottom (top) tessellation rotates, and therefore the column can twist. Also, we can simulate the twist with free-translation of an assembly ($\varphi = \bar{\varphi}$, $F = 0$) by solving the following optimization problem

$$\min_{h_{k,k'}, \varphi_{k,k'}} U_{\text{assembly}} \quad \text{s.t.} \quad \begin{cases} -(\pi - 2\pi/n) < \varphi_{k,k'} < \pi - 2\pi/n, \quad h_{k,k'} > 0, \\ r_{k'} \sum_k \varphi_{k,k'} c_{k,k'} = \bar{\varphi}, \\ \sum_k h_{k,k'} = \sum_k h_{k,k'+1}, \\ \frac{\partial U_{\text{cell},k,k'}(h_{k,k'}, \varphi_{k,k'})}{\partial h_{k,k'}} = \frac{\partial U_{\text{cell},k+1,k'}(h_{k+1,k'}, \varphi_{k+1,k'})}{\partial h_{k+1,k'}}, \\ \frac{\partial U_{\text{cell},k,k'}(h_{k,k'}, \varphi_{k,k'})}{\partial \varphi_{k,k'}} = \frac{\partial U_{\text{cell},k+1,k'}(h_{k+1,k'}, \varphi_{k+1,k'})}{\partial \varphi_{k+1,k'}}. \end{cases} \quad (\text{S23})$$

If *all the columns are the same* (subject to reversed chirality to match the rotation direction of the square in the tessellation), we assume that the minimum energy occurs when all the columns have the same deformation (i.e., the same $h_{k,k'}$ and $\varphi_{k,k'}$). The justification for this assumption is that the tessellation confines that the columns have the same height h and twist angle φ (subject to the opposite sign for different chirality), and for simplification, we ignore the possible bifurcation when different height/twist distributions inside a column induce the same energy. Then, the strain energy can be rewritten as

$$U'_{\text{assembly}}(h, \varphi) = N' U_{\text{column},k'_0}(h, \varphi) + \frac{k_{\text{RS}}}{2} \varphi^2 \quad (\text{S24})$$

In this way, the number of optimization variables is reduced to that for a single column (indexed by k'_0). Then, the compression with free-rotation simulation ($h = \bar{h}$, $T = 0$) is simplified to

$$\min_{h_{k,k'_0}, \varphi_{k,k'_0}} U'_{\text{assembly}} \quad \text{s.t.} \quad \begin{cases} -(\pi - 2\pi/n) < \varphi_{k,k'_0} < \pi - 2\pi/n, \quad h_{k,k'_0} > 0, \\ \sum_k h_{k,k'_0} = \bar{h}, \\ \frac{\partial U_{\text{cell},k,k'_0}(h_{k,k'_0}, \varphi_{k,k'_0})}{\partial h_{k,k'_0}} = \frac{\partial U_{\text{cell},k+1,k'_0}(h_{k+1,k'_0}, \varphi_{k+1,k'_0})}{\partial h_{k+1,k'_0}}, \\ \frac{\partial U_{\text{cell},k,k'_0}(h_{k,k'_0}, \varphi_{k,k'_0})}{\partial \varphi_{k,k'_0}} = \frac{\partial U_{\text{cell},k+1,k'_0}(h_{k+1,k'_0}, \varphi_{k+1,k'_0})}{\partial \varphi_{k+1,k'_0}}. \end{cases} \quad (\text{S25})$$

The twist with free-translation simulation ($\varphi = \bar{\varphi}$, $F = 0$) is simplified to

$$\min_{h_{k,k'_0}, \varphi_{k,k'_0}} U'_{\text{assembly}} \quad \text{s.t.} \quad \begin{cases} -(\pi - 2\pi/n) < \varphi_{k,k'_0} < \pi - 2\pi/n, \quad h_{k,k'_0} > 0, \\ \sum_k \varphi_{k,k'_0} c_{k,k'_0} = \bar{\varphi} \\ \frac{\partial U_{\text{cell},k,k'_0}(h_{k,k'_0}, \varphi_{k,k'_0})}{\partial h_{k,k'_0}} = \frac{\partial U_{\text{cell},k+1,k'_0}(h_{k+1,k'_0}, \varphi_{k+1,k'_0})}{\partial h_{k+1,k'_0}}, \\ \frac{\partial U_{\text{cell},k,k'_0}(h_{k,k'_0}, \varphi_{k,k'_0})}{\partial \varphi_{k,k'_0}} = \frac{\partial U_{\text{cell},k+1,k'_0}(h_{k+1,k'_0}, \varphi_{k+1,k'_0})}{\partial \varphi_{k+1,k'_0}}. \end{cases} \quad (\text{S26})$$

Calibration of stiffness. By solving Eq. (S12) and using $T = \partial U_{\text{cell}}(\bar{h}, \varphi) / \partial \varphi$ for a series of $\bar{h} \in (h_0, h_1)$, we can obtain the curve of force T versus displacement u (that is, the absolute change of height) with given stiffness k_b , k_t , k_r that are defined in the Methods. We determine the values of stiffness for the cells of different materials (say, the red, white, and yellow cells in the Main Text) based on the experimental compression loading curves (see Fig. S16). For each cell, we extract three representative quantities from the experimental curve, that is, the peak force F_p , the minimum force F_m , and the displacement to the second stable state u_s . Specifically, for the red cell, we have $F_p^{\text{R}} = 0.9482$ N, $F_m^{\text{R}} = -0.1455$ N, and $u_s^{\text{R}} = 15.3339$ mm; for the white cell, we have $F_p^{\text{W}} = 2.2475$ N, $F_m^{\text{W}} = -0.0128$ N, and $u_s^{\text{W}} = 10.2807$ mm; for the yellow cell, we have $F_p^{\text{Y}} = 3.8273$ N, $F_m^{\text{Y}} = -0.1630$ N, and $u_s^{\text{Y}} = 11.3137$ mm. Then, we use the function `fgoalattain` in MATLAB R2023b to solve the following multiobjective goal attainment problem:

$$\min_{k_b, k_t, k_r, \gamma} \gamma \quad \text{s.t.} \quad \begin{cases} \mathbf{f}(k_b, k_t, k_r) - \text{goal} \leq \text{weight} \cdot \gamma, \\ F_m(k_b, k_t, k_r) \leq 0. \end{cases} \quad (\text{S27})$$

The goal is an array containing the three representative quantities for a cell. The map $\mathbf{f}(k_b, k_t, k_r) = (F_p, F_m, u_s)$ is determined by solving Eq. (S12) and using $T = \partial U_{\text{cell}}(\bar{h}, \varphi) / \partial \varphi$ for a series of $\bar{h} \in (h_0, h_1)$. Setting a component of the weight vector to zero causes the corresponding goal constraint to be treated as a hard constraint rather than a goal constraint. According to our observation, with the current surrogate model, it is hard to match these three quantities at the same time. Therefore, we set $\text{weight} = (0, 100, 0.1)$ for the precise match of peak force F_p and a preference of better matching of the displacement to the second stable state u_s . With the calibrated stiffness, we can obtain the simulation loading curves of the red, white, and yellow cells (see Fig. S16).

S6 Magnetically actuated robotic metamaterials

The cylindrical neodymium permanent magnets that ensure the integrity of the assembly and enable the locomotion mode of the metamaterial are high strength N50-grade, with out-of-plane magnetization, 2 mm diameter and 0.5 mm thickness (Supermagnetman D1002-10). The soft square magnetic plates have a 16 mm side length and a thickness of 2 mm. They are made of an 80% by weight compound of 25 micron Nd-Pr-Fe-B alloy powder (Magnequench MQFP 15-7 20065-088) and silicone rubber (Ecoflex 00-30). A high-precision digital scale (Hanchen model HC-220.4) is used to ensure consistent powder concentration. The mixture is poured into 3D printed molds and is allowed to cure for 12 hours in standard room conditions. Subsequently, each soft plate is removed from the mold and placed inside an impulse magnetizer (ASC Scientific MODEL IM-10-30) which is charged to a voltage of 420 V before the magnetization event is initiated. Both the cylindrical magnets and the soft plates are attached to the metamaterial assembly using a high-strength adhesive compound (Loctite Super Glue Ultra Gel).

The 3 dimensional Helmholtz coil system comprises six individual coils (two for each axis) made of 10 gauge square magnet wire (Extended Data Figs. 6a and 6c). Each of the six coils consists of an inner and outer circular winding connected in series. The geometrical characteristics of each winding are presented in Table S1. An epoxy adhesive (Wakefield BT-301) is used to provide additional robustness and enhance the heat dissipation performance.

Axis	Position	Mean radius [cm]	Number of turns	Offset from origin [cm]
x	outer	15.2	56	± 9.7
x	inner	16.5	64	± 7.2
y	outer	12.2	48	± 8.5
y	inner	13.5	54	± 6.3
z	outer	10.0	40	± 6.6
z	inner	11.1	40	± 4.8

Table S1: **3-D Helmholtz coil winding characteristics.**

To precisely generate the magnetic field, a modular 25-kW power converter employing 100-V top cooled power MOSFET devices (Infineon IPTC014N10NM5) was designed and implemented (Extended Data Figs. 6b and 6d). Each of the six winding pairs is independently driven by an H-bridge submodule switching at 10 kHz that outputs a pulsed voltage waveform at an effective switching frequency of 20 kHz. To reduce the semiconductor conduction loss and increase the conversion efficiency, every switch is implemented by two power MOSFETs connected in parallel. Each submodule comprises its own copper heatsink and two fans provide forced convection cooling. The coil currents are sensed locally in each submodule using shunt resistors (Bourns CSS2H-5930K-1L00FE). The measured current values are sampled every 100 μs by a microcontroller control card (Texas Instruments TMS320F2837) that implements a PI-based closed loop current-control scheme (Extended Data Fig. 6e). In this way, the coil currents are precisely controlled and they are not affected by changes in the operating conditions such as the increased coil resistance resulting from a rise in the copper-winding temperature. The power converter is energized by a power supply unit (BK PRECISION 9117) that provides a DC voltage up to 80 V to the drive input. A dc-link capacitance is implemented using solid polymer aluminum capacitors and it is evenly distributed among the submodules. The actual coil currents are measured and logged in real time in an oscilloscope (Tektronix DPO4104) using current probes (Tektronix TCP0030A). Finally, we performed the magnetic field calibration by imposing a constant current through every coaxial coil pair and employing a vector gaussmeter instrument (Gaussmeter Model VGM, AlphaLab Inc) to measure the magnetic field strength.

S7 On thermoregulation of buildings

Thermoregulating buildings is a growing and urgent challenge in a world that faces rising temperatures and increasingly frequent extreme heat and cold waves. Cooling and heating buildings currently consumes about 10% of energy in the US (<https://www.eia.gov/>), with cooling loads expected to grow dramatically by 2050 due to climate change, even as air conditioning is increasingly regarded as a non-ideal solution due to its cost, energy usage, CO₂ emissions, and net heat generation. Passive radiative cooling and heating of buildings are sustainable alternatives or complements

to active thermoregulation ([S2, S3]). By optically tailoring building envelopes to reflect sunlight and radiate heat through the atmosphere to space, or harness solar heat, buildings can be cooled or heated without any energy usage and CO₂ emissions. Recent years have seen major academic and industrial efforts on this front. Yet, current designs are often static, and thus suboptimal in seasonally varying environments, e.g. cool white roofs in the winter. On the other hand, adaptive designs (e.g. thermochromic envelopes), are often limited in their optical properties, tunability, and materials. Thus, optimal thermoregulation of buildings in complex environments remains a challenge, while holding promise for massive energy savings, thermal comfort and emissions reductions.

We address this need with a reconfigurable optomechanical design – the multimodal and multistable origami metamaterial equipped with radiative cooling and/or selectively solar absorbing panels. By continuously morphing between folded and deployed stable states, the optically augmented assembly can attain any intermediate states between radiative cooling and solar heating modes, and also trap different thicknesses of air, similar to piloerection in animals ([S4]). The first of these can radiatively thermoregulate buildings, while the second can serve as tunable insulation.

We proof this concept using a prototype as shown in Extended Data Fig. 7. Preliminary models and estimates from the literature (<https://web.ornl.gov/sci/buildings/tools/cool-roof/>) indicate that the radiative mode origami assembly on roofs (784 m² area residential buildings with average insulation) can reduce air conditioning loads by 400-7000 kWh per year relative to traditional dark roofs, and wintertime heating loads by 500-1500 MJ compared to cool roofs, depending on the climate. The convective functionality could enhance these values by 16-30%.

S8 Preisach model of the modular dipoles

The mechanical hysterons are achieved with the origami dipoles. The relationship between the dipole height and the input force, in analogy to the relationship between the magnetization of a magnetic material and the magnetic field for hysteresis, can be mathematically expressed by

$$\tilde{h}(F; F^L, F^R) = \begin{cases} h_1, & F \leq F^L, \\ h_0, & F \geq F^R, \\ h_{\text{last}}, & F^L < F < F^R, \end{cases} \quad (\text{S28})$$

in which h_{last} is the height of a dipole in the last loading step. In our demonstration, we define the hysterons by extracting the data from the experimental measurement illustrated in Fig. 5c in the Main Text. The values of the parameters F^L and F^R correspond to the valley and peak forces in the loading curves, respectively. The parameters h_1 and h_0 correspond to the deployed and folded heights, respectively. Specifically, we have $F^L = -0.17$ N, -0.15 N, and -0.24 N, $F^R = 0.87$ N, 1.98 N, and 3.50 N for the red, white, and yellow dipoles, respectively. For all three dipoles, we assign the same bivalued height with $h_1 = 28.3$ mm and $h_0 = 12.6$ mm. Finally, the mechanical Preisach model of the dipole series becomes the summation of the three individual operators under the same input force, expressed as

$$h(F) = \sum_{k=1}^3 \tilde{h}(F; F_k^L, F_k^R). \quad (\text{S29})$$

Equation (S28) is used to generate the three mini plots in Fig. 6c (left) in the Main Text. Equation (S29) is used to generate the large plots in Fig. 6c (right) in the Main Text.

S9 Inverse layout design for the modular cell

A min-max topology optimization formulation. We apply an optimization framework to inversely design the modular unit given a prescribed force-displacement relationship. A min-max optimization formulation is presented to optimize the topology of the rod-based lattice at the unit-cell level. The focus is to understand lattice nodal connectivity. The topology design consists of determining the cross-sectional areas of the rod members using the Ground Structure (GS) Method [S5]. Seeking rod layouts of satisfying the prescribed force-displacement relationship at a certain Degree of Freedom (DOF), we minimize the maximum error between the actual reaction force factors and the prescribed ones:

$$\begin{aligned} & \min_{\mathbf{x}} \max_{u^p} J = [\chi(\mathbf{x}, \mathbf{u}_p(\mathbf{x})) - \chi^*(d^*)]^2, \quad p = 1, \dots, n \\ \text{s.t.} & \quad \begin{cases} \sum \mathbf{L}^T \mathbf{x} - V_{\text{max}} \leq 0 \\ 0 \leq x_e \leq x_{\text{max}}, \quad e = 1, \dots, m \end{cases} \\ \text{with} & \quad \begin{cases} \mathbf{T}(\mathbf{x}, \mathbf{u}_p(\mathbf{x})) = \chi(\mathbf{x}, \mathbf{u}_p(\mathbf{x})) \mathbf{f}_0 \\ \mathbf{f}_0^T \mathbf{u}_p(\mathbf{x}) = d^* \end{cases} \end{aligned} \quad (\text{S30})$$

The objective function is the error between the actual force response χ and the prescribed force response χ^* [S6]. The associated prescribed displacement (at certain DOFs) is denoted by d^* . The index p denotes the specific data

point from a data set, including a total number n of prescribed data points. More specifically speaking, each of the prescribed data points is denoted as $[d^*, \chi^*]$. We define \mathbf{x} as the vector of the design variables representing the cross-sectional areas of the rod members in the undeformed configurations, and \mathbf{u}_p is the vector of nodal displacements. \mathbf{L} is the vector of the rod-member lengths in the undeformed configurations, V_{\max} is a limit on the total volume of the rod layout in the undeformed configuration, index e denotes a specific rod member from a total number of m rods, x_{\max} is the upper bound of the undeformed cross-sectional area for rod members, T is the internal forces vector, and f_0 is a unit reference force vector with all zero components except at the DOF where u_p is prescribed. Note that we allow the rod cross-sectional areas to reduce to zero, and the resulting singular tangent stiffness matrix \mathbf{K} is prevented using a regularization scheme inspired by the damped Newton method, i.e., $\mathbf{K}^\eta = \mathbf{K} + \eta\mathbf{I}$ where η is the damped Newton parameter defined as $\eta_0 = 10^{-8}$ multiplied by the means of the diagonal of \mathbf{K} [S7]. To solve the nonlinear state equations in Eq. (S30), we use an incremental-iterative nonlinear solution scheme [S8, S9]. The scheme is based on the modified generalized displacement control method (MGDCM) [S10], which is a variant of the class of arc-length methods. The method can follow equilibrium paths with snap-through and snap-back behaviors.

Using formulation (S30), we seek to understand the nodal connectivity of a 4-gon cell with desired bistable behavior. Given three data points on a target equilibrium trajectory in Fig. S12a and the corresponding boundary and loading conditions in Fig. S12b, the optimizer extracts the optimal rod layout from the initial GS shown in Fig. S12c(left). The optimal rod-based design as shown in Fig. S12c(right) reassembles the 4-gon cell layout in Fig. 1e.

Non-self-adjoint sensitivity analysis. We derive the sensitivity of the objective function J in Eq. (S30) with respect to the design variable \mathbf{x} . Let's start by taking the total derivative of J as follows:

$$\frac{dJ}{dx_e} = 2 [\chi(\mathbf{x}, \mathbf{u}_p(\mathbf{x})) - \chi^*(d^*)] \frac{d\chi(\mathbf{x}, \mathbf{u}_p(\mathbf{x}))}{dx_e} \quad (\text{S31})$$

To evaluate the term $d\chi(\mathbf{x}, \mathbf{u}_p(\mathbf{x}))/dx_e$ in Eq. (S31), we differentiate one of the state equations $\mathbf{T}(\mathbf{x}, \mathbf{u}_p(\mathbf{x})) = \chi(\mathbf{x}, \mathbf{u}_p(\mathbf{x})) \mathbf{f}_0$ with respect to x_e :

$$\frac{\partial \mathbf{T}(\mathbf{x}, \mathbf{u}_p(\mathbf{x}))}{\partial x_e} + \left[\frac{\partial \mathbf{T}(\mathbf{x}, \mathbf{u}_p(\mathbf{x}))}{\partial \mathbf{u}_p} \right]^T \frac{d\mathbf{u}_p(\mathbf{x})}{dx_e} = \frac{d\chi(\mathbf{x}, \mathbf{u}_p(\mathbf{x}))}{dx_e} \mathbf{f}_0, \quad (\text{S32})$$

where $\partial \mathbf{T}(\mathbf{x}, \mathbf{u}_p(\mathbf{x}))/\partial \mathbf{u}_p(\mathbf{x}) = \mathbf{K}_T(\mathbf{x}, \mathbf{u}_p(\mathbf{x}))$ which is the tangent stiffness matrix. From Eq. (S32) we obtain

$$\mathbf{f}_0^T \frac{d\mathbf{u}_p}{dx_e} = \mathbf{f}_0^T (\mathbf{K}_T)^{-1} \frac{d\chi}{dx_e} \mathbf{f}_0 - \mathbf{f}_0^T (\mathbf{K}_T)^{-1} \frac{\partial \mathbf{T}}{\partial x_e}. \quad (\text{S33})$$

According to the other state equation $\mathbf{f}_0^T \mathbf{u}_p(\mathbf{x}) = d^*$, and thus we know

$$\mathbf{f}_0^T \frac{d\mathbf{u}_p}{dx_e} = 0. \quad (\text{S34})$$

By substituting Eq. (S33) into Eq. (S34), we obtain the analytical expression of $d\chi/dx_e$ as

$$\frac{d\chi}{dx_e} = \frac{(\frac{\partial \mathbf{T}}{\partial x_e})^T \mathbf{u}_0}{\mathbf{f}_0^T \mathbf{u}_0} \quad (\text{S35})$$

where $\mathbf{u}_0 = (\mathbf{K}_T)^{-1} \mathbf{f}_0$. By substituting Eq. (S35) into Eq. (S31), we obtain the final expression of the sensitivity

$$\frac{dJ}{dx_e} = 2 [\chi - \chi^*] \frac{(\frac{\partial \mathbf{T}}{\partial x_e})^T \mathbf{u}_0}{\mathbf{f}_0^T \mathbf{u}_0} \quad (\text{S36})$$

Since there is no need for solving extra adjoint problems during the derivation of Eq. (S36), the sensitivity presented here is quite simple and effective.

S10 Preferred modular cell design features

We elaborate upon the preferred design features for the Kresling cells in terms of three aspects: chirality, energy barrier, and kinematic compatibility. Using the case study of a two-layer assembly test, we demonstrate how considering the three aspects leads to the desired multimodal deformation (e.g., assembly twist and height shrinkage).

Chirality: we design unit cells with opposite chirality, which allows us to have cells that can twist in the clockwise (cw) direction while other cells twist in the counterclockwise (ccw) direction (Fig. S13a). Then, we assemble cells with proper chirality arrangement, based on Equation (1) (Main Text), into 3D assemblies to enable desired

multimodal deformation. For instance, the two-layer assembly in Fig. S13c has the proper chirality arrangement satisfying Equation (1). By applying an 83° twist in the counterclockwise direction from state (1) to state (2), the assembly achieves the desired deformation, i.e., the bottom layer of cells folds and the tessellation contracts in-plane.

Energy barrier: we design cells with distinguishable energy barriers. The energy barriers of the cell can be tuned by controlling the material's stiffness at the joints. For instance, since the white cell has a stiffer joint than the red cell, the energy barrier of the white cell is higher than that of the red cell (Fig. S13b). By arranging cells with different energy barriers, we can control the folding sequence of the layers in the assembly. For example, there are two potential kinematic folding paths from state (2) to state (3) in Fig. S13c: **1.** the white-cell layer deploys while the red-cell layer remains deployed; **2.** the red-cell layer folds while white-cell layer remains folded. Since the white cell has a higher energy barrier than the red cell, the red cell will deform before the white cell. Thus, the folding path **2** is preferable. As a result, we achieve a controllable folding sequence and the height shrinks in the end state.

Kinematic compatibility: we design the twist of the Kresling unit to be kinematically compatible with the twist of the tessellations on top and bottom. The maximum rotation angle of the rotating-square tessellation is 90° . Thus, the change of rotation angle $\Delta\varphi$ for the Kresling unit is designed to be less or equal to 90° . The $\Delta\varphi$ is defined as follows:

$$\Delta\varphi = \varphi_0 - \varphi_1, \quad \varphi_1 = \arccos\left(\frac{h_1^2 - h_0^2}{4r^2} \sec \frac{\pi}{n}\right) - \frac{\pi}{n}, \quad \varphi_0 = \pi - \frac{2\pi}{n} - \varphi_1. \quad (\text{S37})$$

For 6-gon cells used in the Main Text, we define deployed height $h_1 = 28.3$ mm, folded height $h_0 = 12.6$ mm, polygon radius $r = 16.8$ mm, polygon edge number $n = 6$, and then we obtain $\Delta\varphi = 83^\circ < 90^\circ$. Moreover, those geometry parameters need to satisfy the following design constraint to avoid the locking stage where diagonal rods collide in the folded state [S11]:

$$|h_1^2 - h_0^2| \leq 4r^2 \cos^2 \frac{\pi}{n}. \quad (\text{S38})$$

S11 Captions of supplementary videos

Supplementary Video 1: Twist experiment.

Supplementary Video 2: Linear displacement experiment.

Supplementary Video 3: Multimodal metamaterial simulations.

Supplementary Video 4: Plug-and-play: reconfigurable assemblies.

Supplementary Video 5: Magnetic robot transformer.

Supplementary Video 6: Non-commutative state transition.

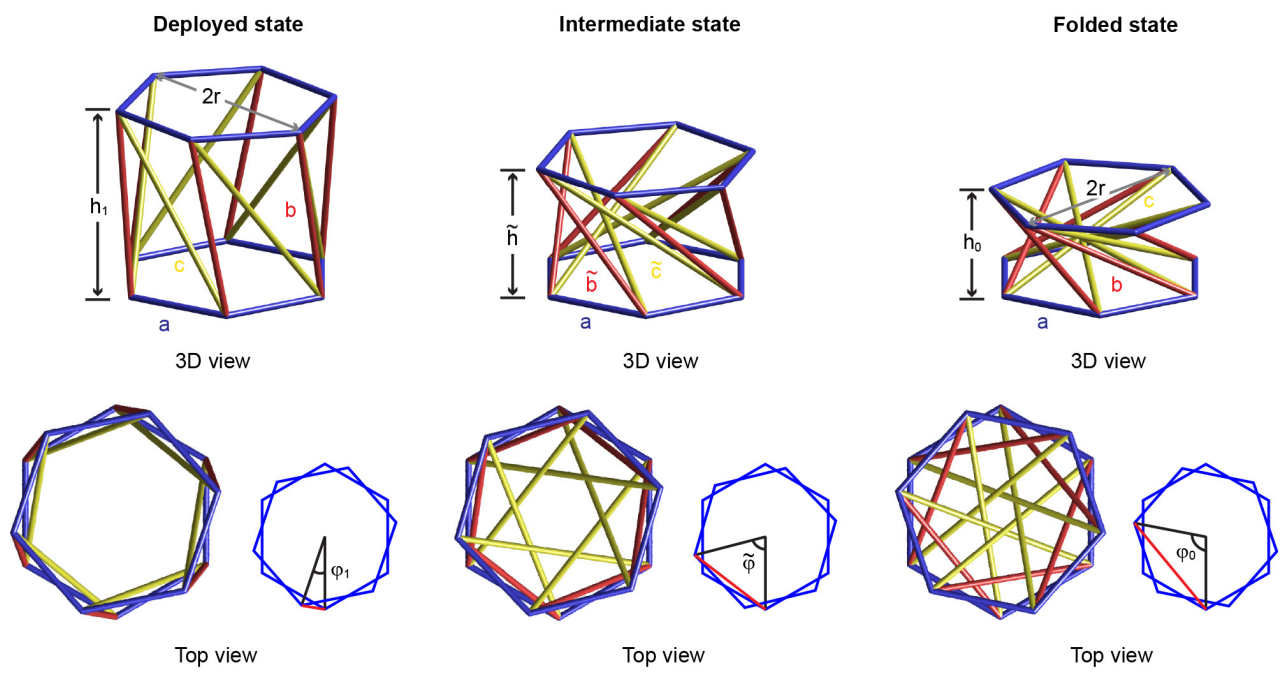


Figure S1: Kresling cell at its deployed (left), intermediate (middle), and folded (right) states.

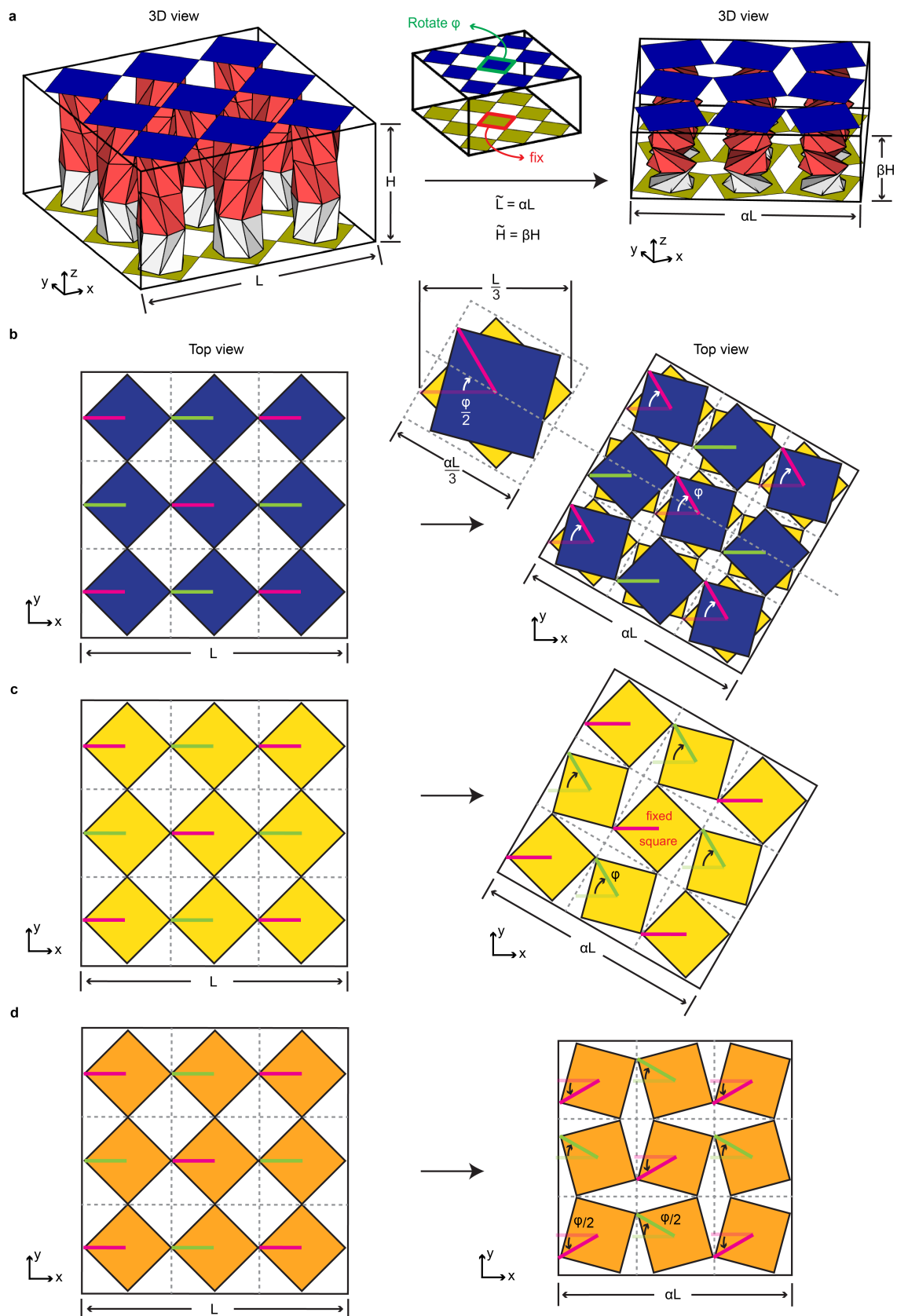


Figure S2: **Geometry of the chiral assembly (shown with the surrogate origami model).** **a**, The undeformed assembly occupies an $L \times L \times H$ cuboid (left). After deformation, the size of the cuboid becomes $\alpha L \times \alpha L \times \beta H$ (right). **b**, Deformation of the top (blue) tessellation with the bottom (yellow) tessellation as a reference. **c**, Deformation of the bottom tessellation. **d**, Deformation of a standard rotating-square tessellation.

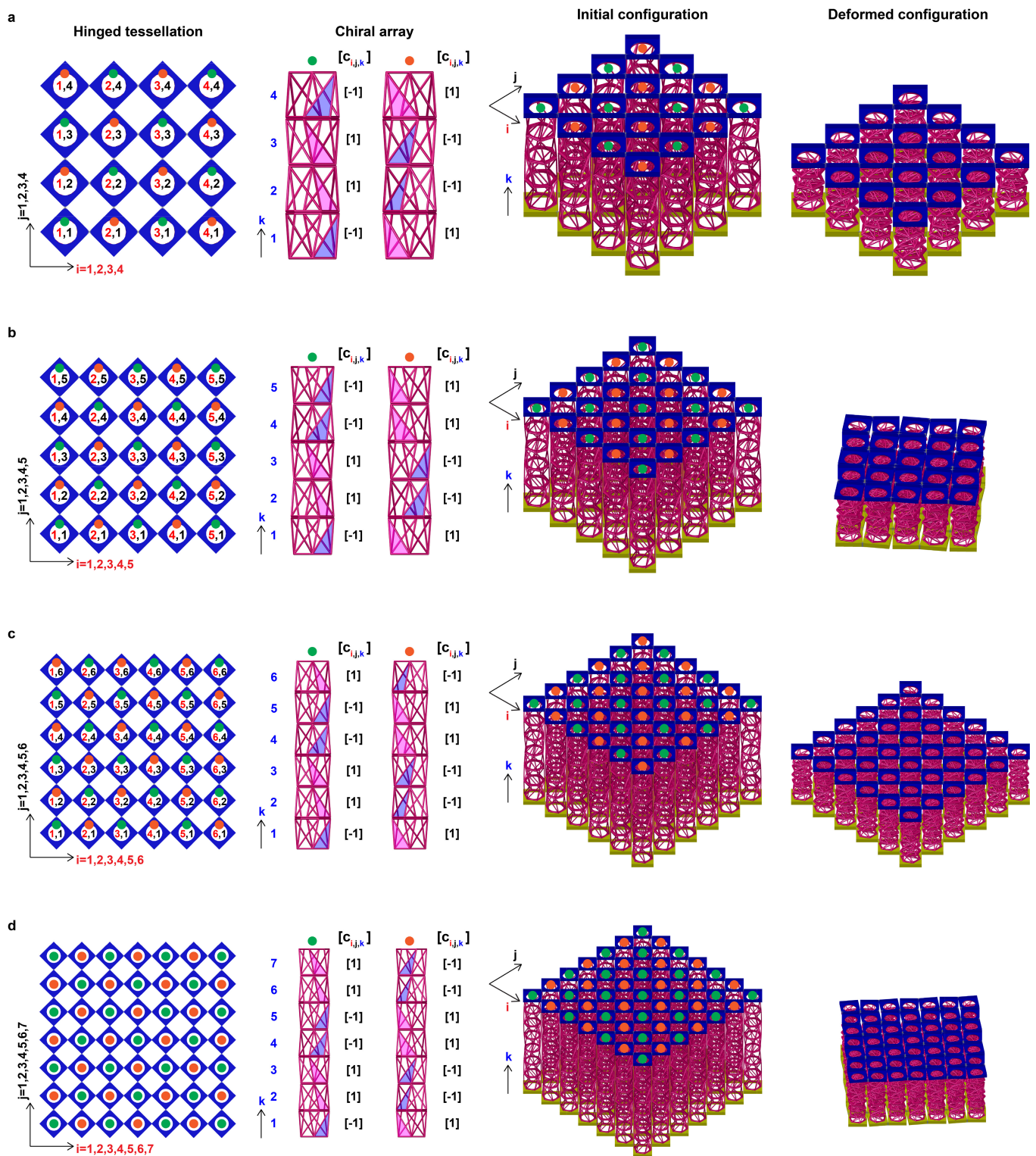


Figure S3: Chirality assignments and corresponding deformation mechanisms for assemblies with increasing system sizes. a-d, Assemblies consisting of various modular units, $4 \times 4 \times 4$, $5 \times 5 \times 5$, $6 \times 6 \times 6$, $7 \times 7 \times 7$, respectively.

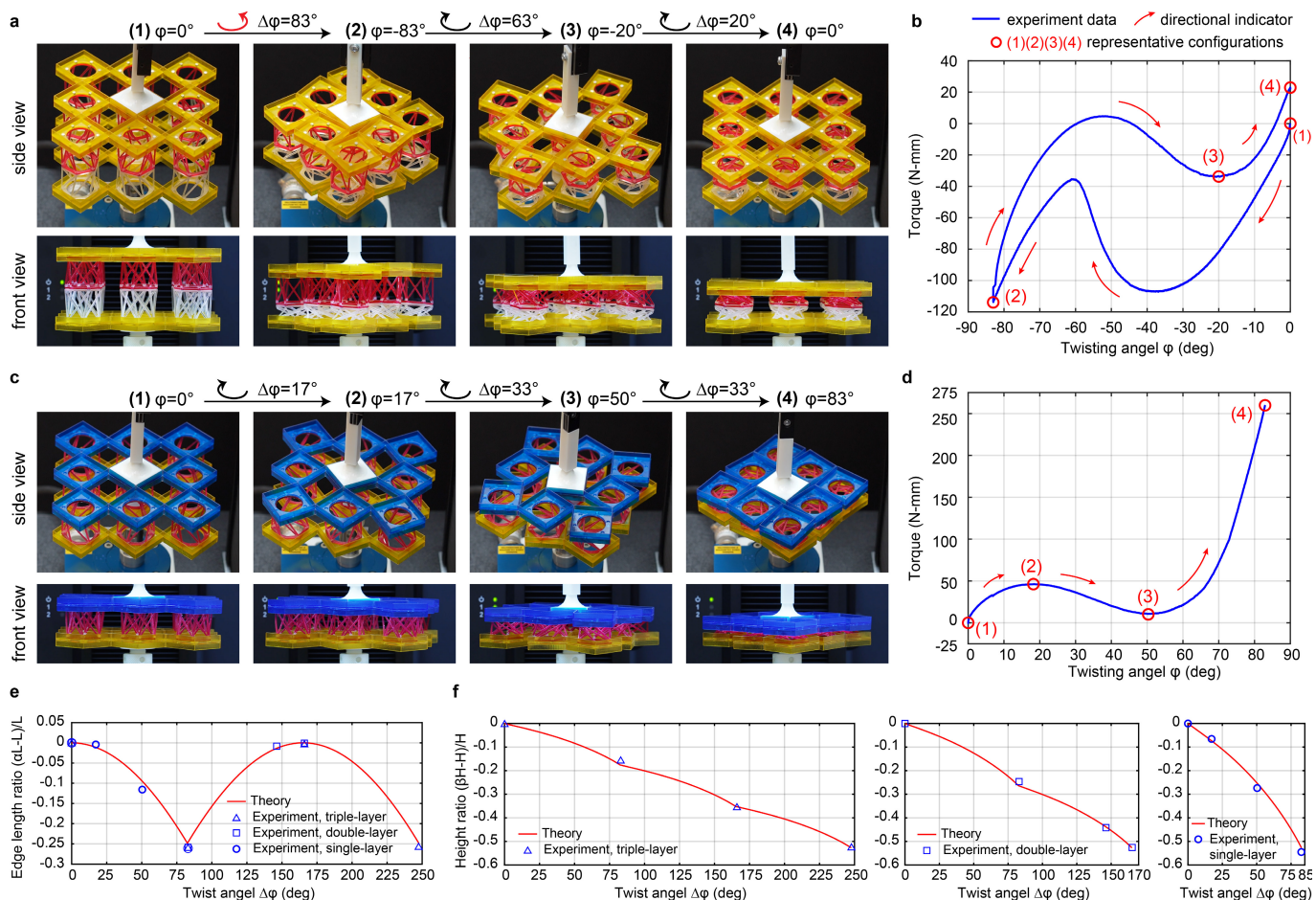


Figure S4: **Alternative tests applying twists with free-translation.** **a**, Four representative configurations of the double-layer assembly test and **b**, the corresponding torque versus twist angle plot. **c**, Four representative configurations of the single-layer assembly test and **d**, the corresponding torque versus twist angle plot. **e**, Assembly edge length change ratio as a function of the twist angle, comparing theory with experiments for the triple-layer, double-layer, and single-layer assemblies, respectively. **f**, Assembly height change versus twist angle. Comparison between theory and experiments on the triple-layer assembly (left), the double-layer assembly (middle), and the single-layer assembly (right), respectively.

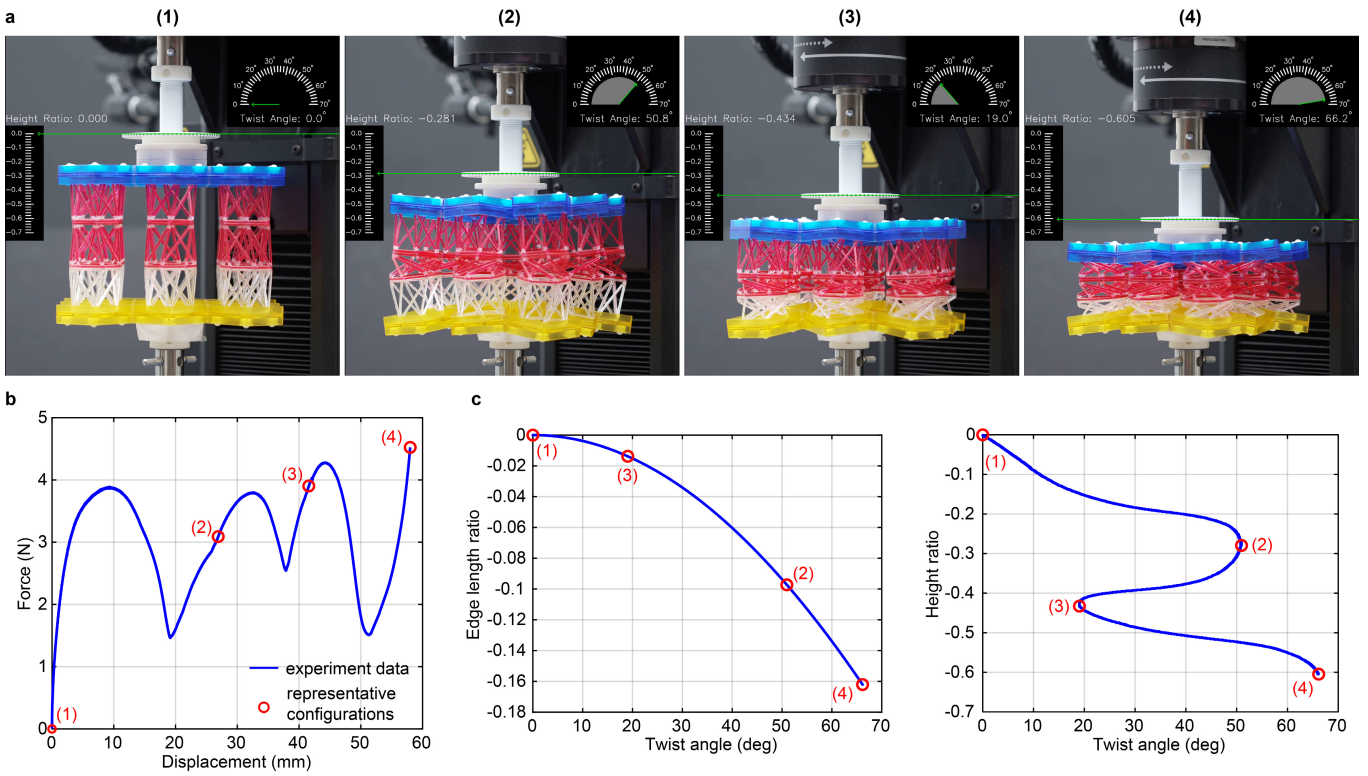


Figure S5: **Linear displacement test with BC#1.** **a**, Four representative configurations. In each inset, the vertical scale bar indicates the height change ratio of the assembly, and the arc scale bar shows the twist angle of the assembly. **b**, Measured force-displacement curve with labels of the four representative states. **c**, Assembly edge length change versus the twist angle (left), assembly height change versus twist angle (right).

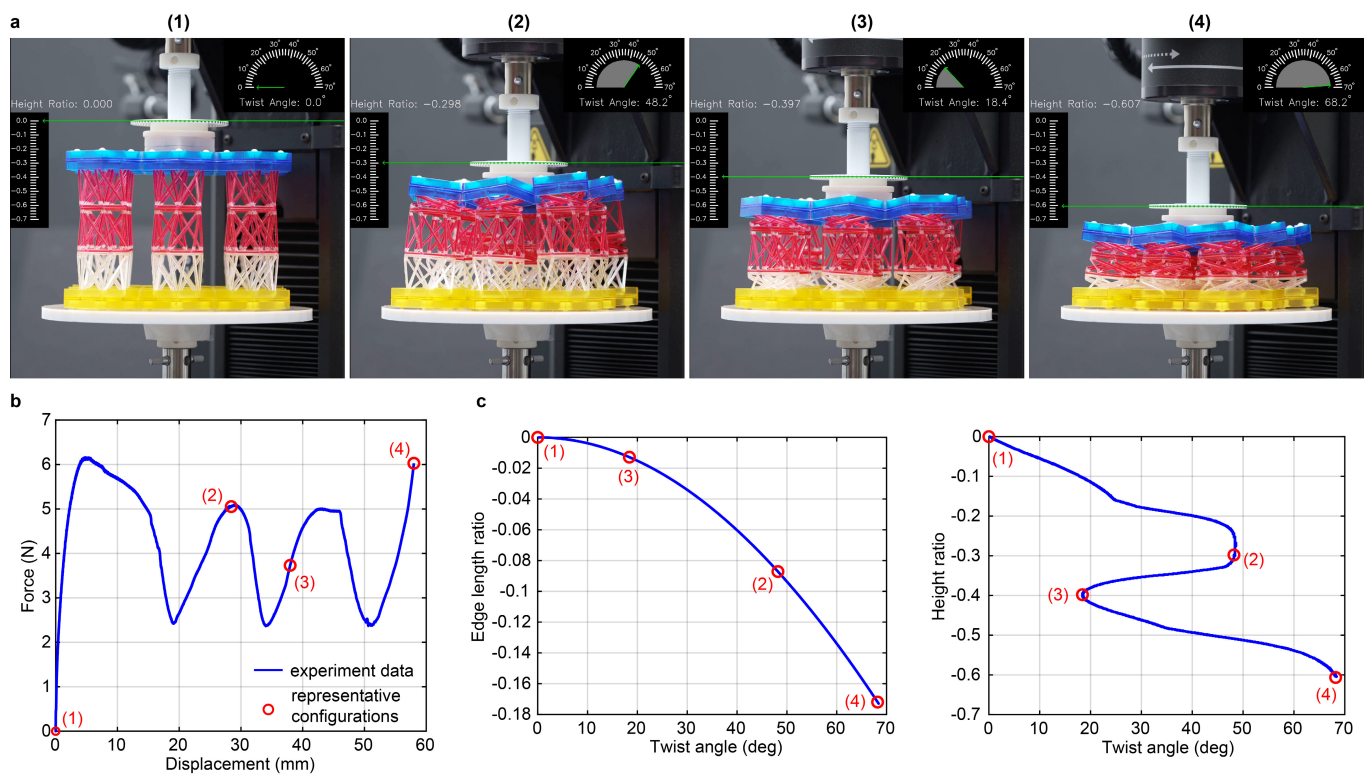


Figure S6: **Linear displacement test with BC#2.** **a**, Four representative configurations. **b**, Measured force-displacement curve. **c**, Assembly edge length change versus twist angle (left), assembly height change versus twist angle (right).

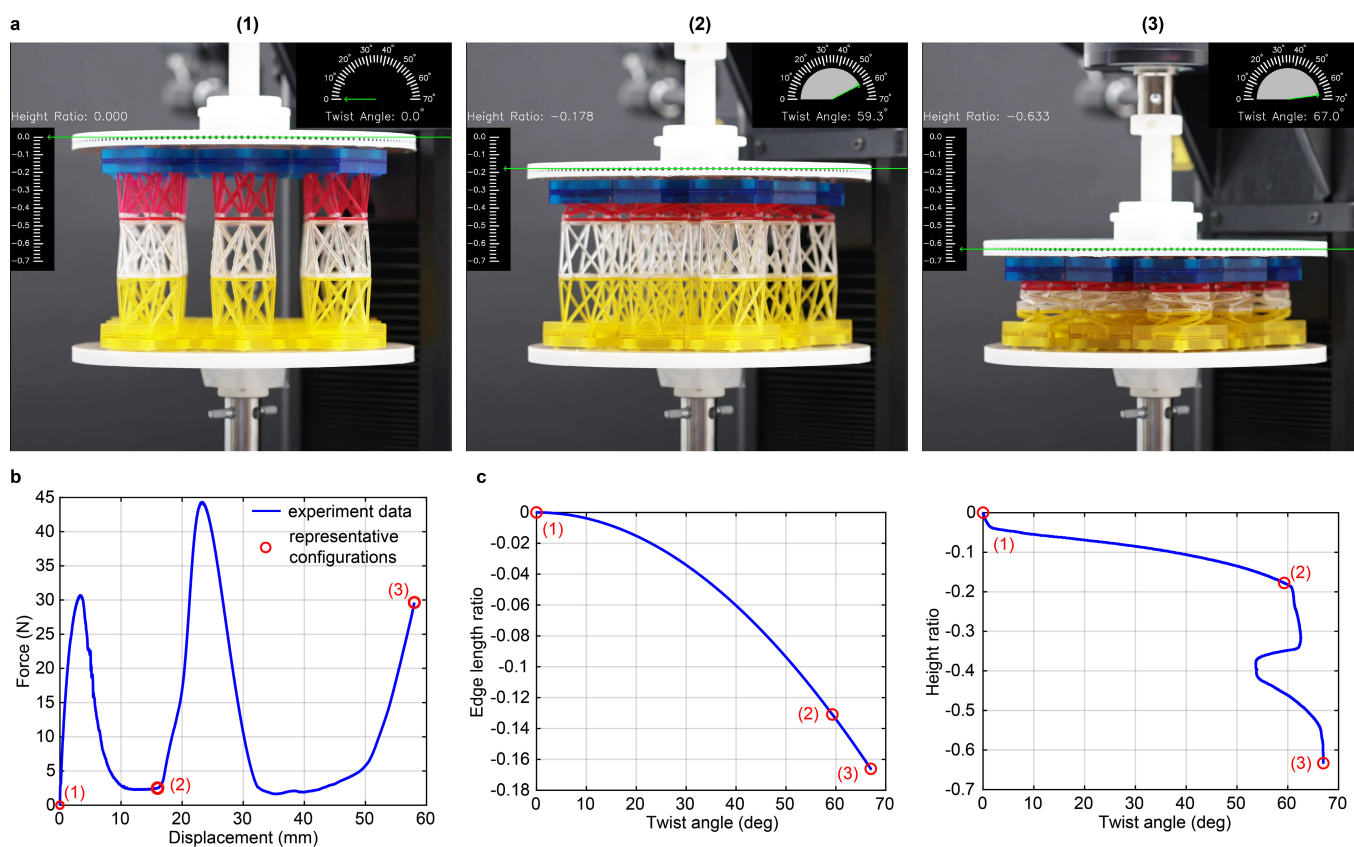


Figure S7: **Linear displacement test for the assembly composed of functionally graded cells.** **a**, Three representative configurations. **b**, Measured force-displacement curve. **c**, Assembly edge length change versus twist angle (left), assembly height change versus twist angle (right).

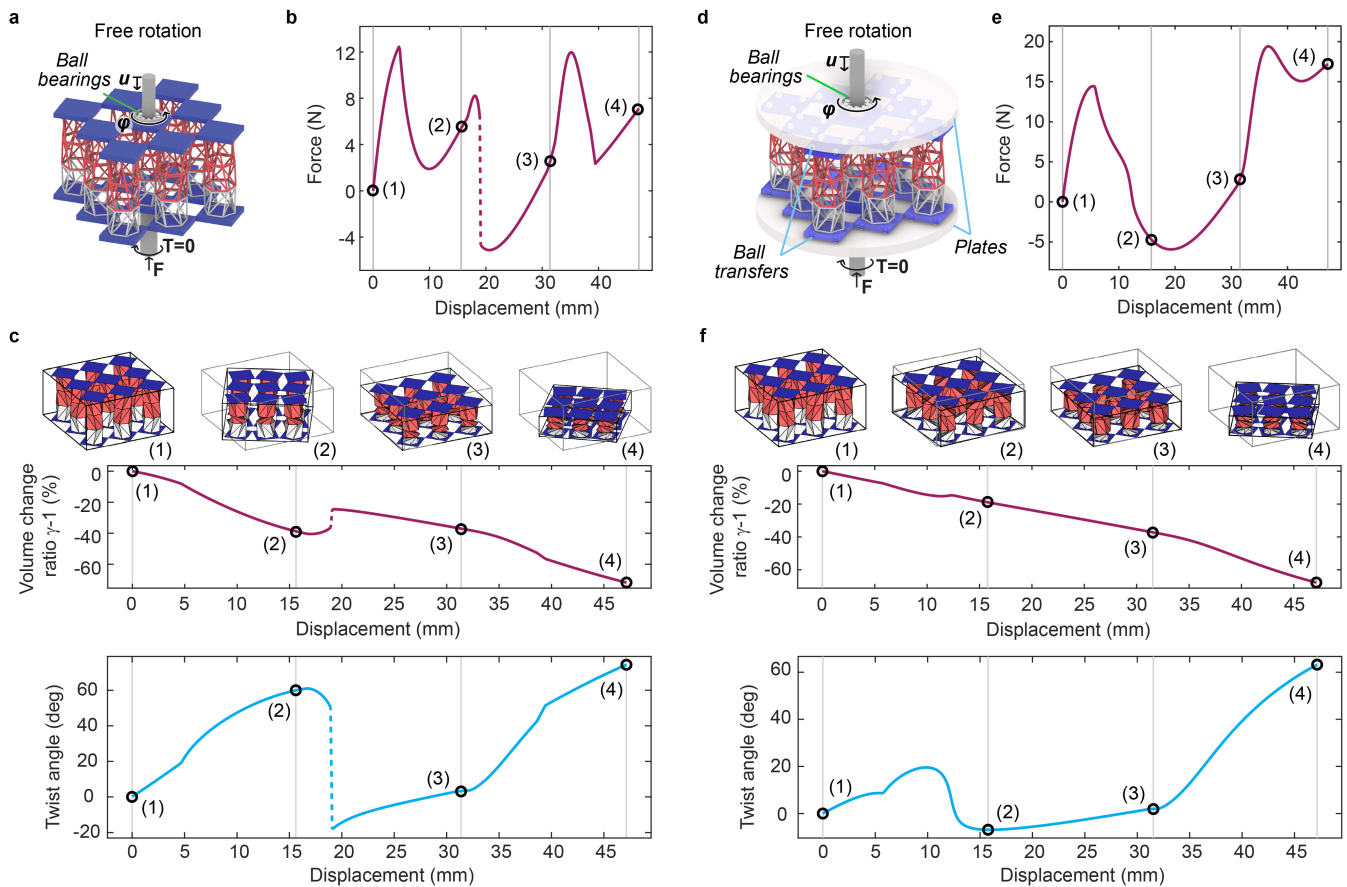


Figure S8: **Linear displacement simulations of the modular assembly considering different boundary conditions.** **a**, Simulation setup with no plates. **b**, Curve of force versus displacement. **c**, Curves of volume change ratio and twist angle versus displacement, and deformation snapshots (1)–(4). The dashed lines represent the sudden change of configuration induced from mechanical instability. **d**, Simulation setup with top and bottom plates. **e**, Curve of force versus displacement. **f**, Curves of volume change ratio and twist angle versus displacement, and deformation snapshots (1)–(4).

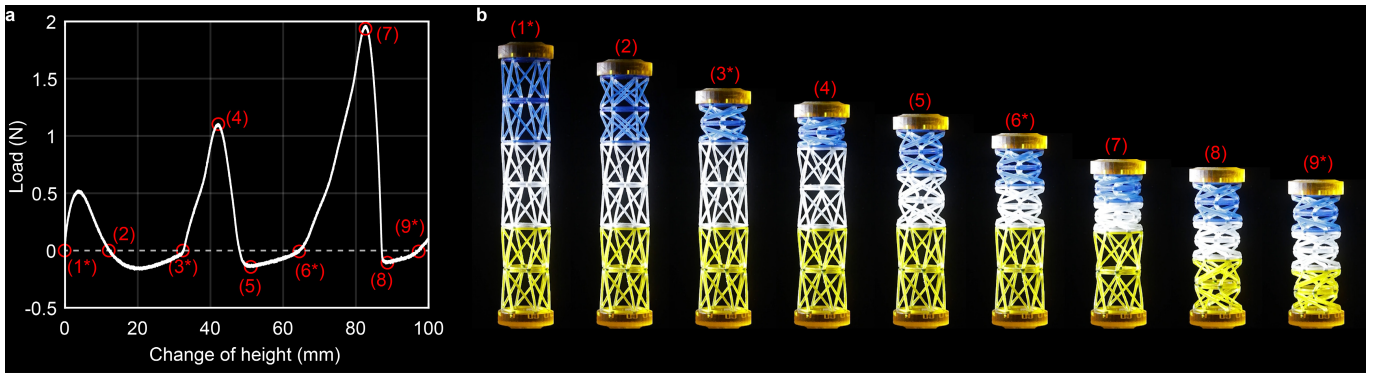


Figure S9: **Modular array with three dipoles.** **a**, Measured load-displacement curves. **b**, Representative configurations.

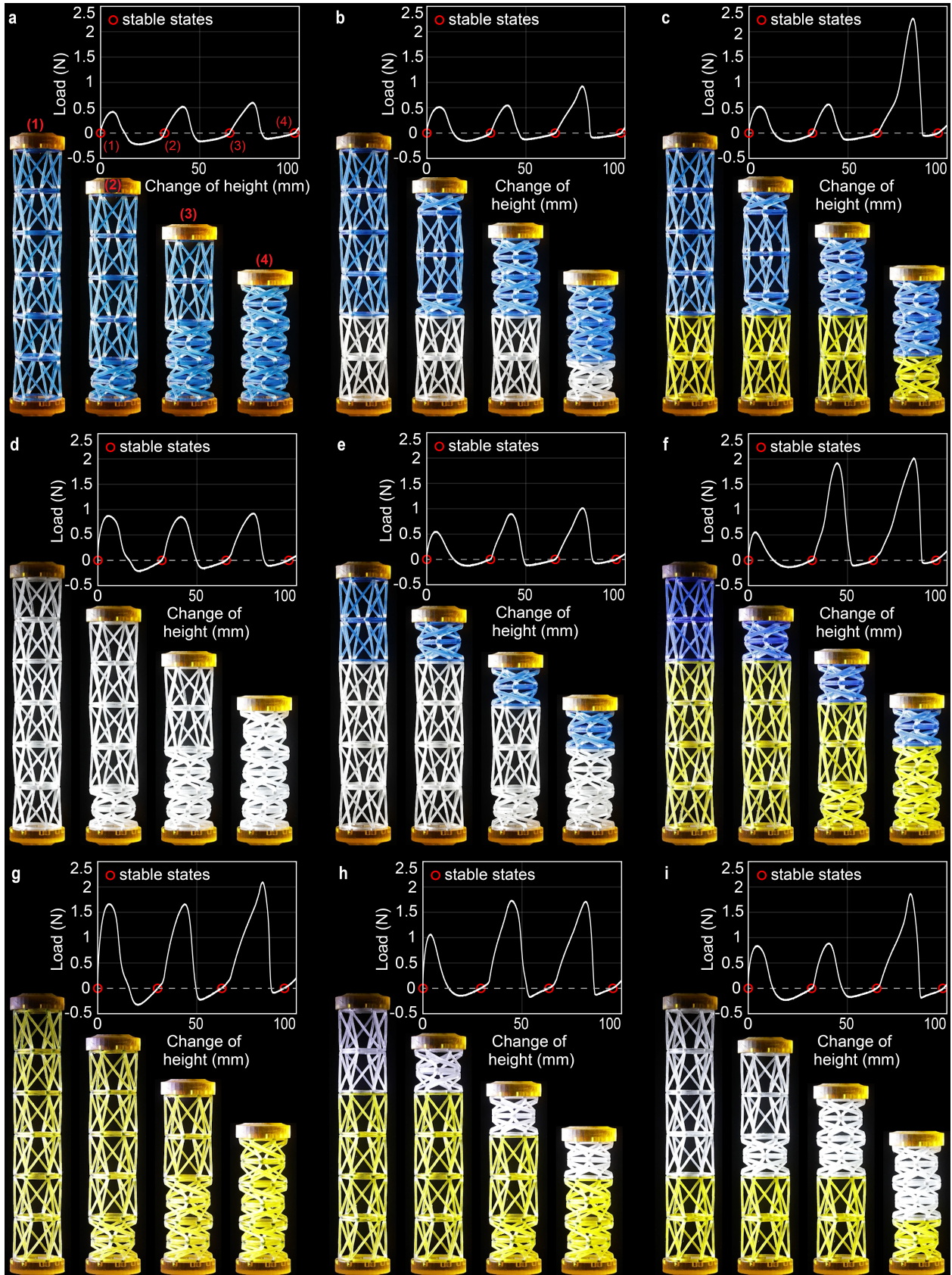


Figure S10: Reconfigurable modular array with multiple stable states and tunable mechanical responses. a-i, Nine combinations of modular cells, corresponding stable configurations and measured load-displacement curves.

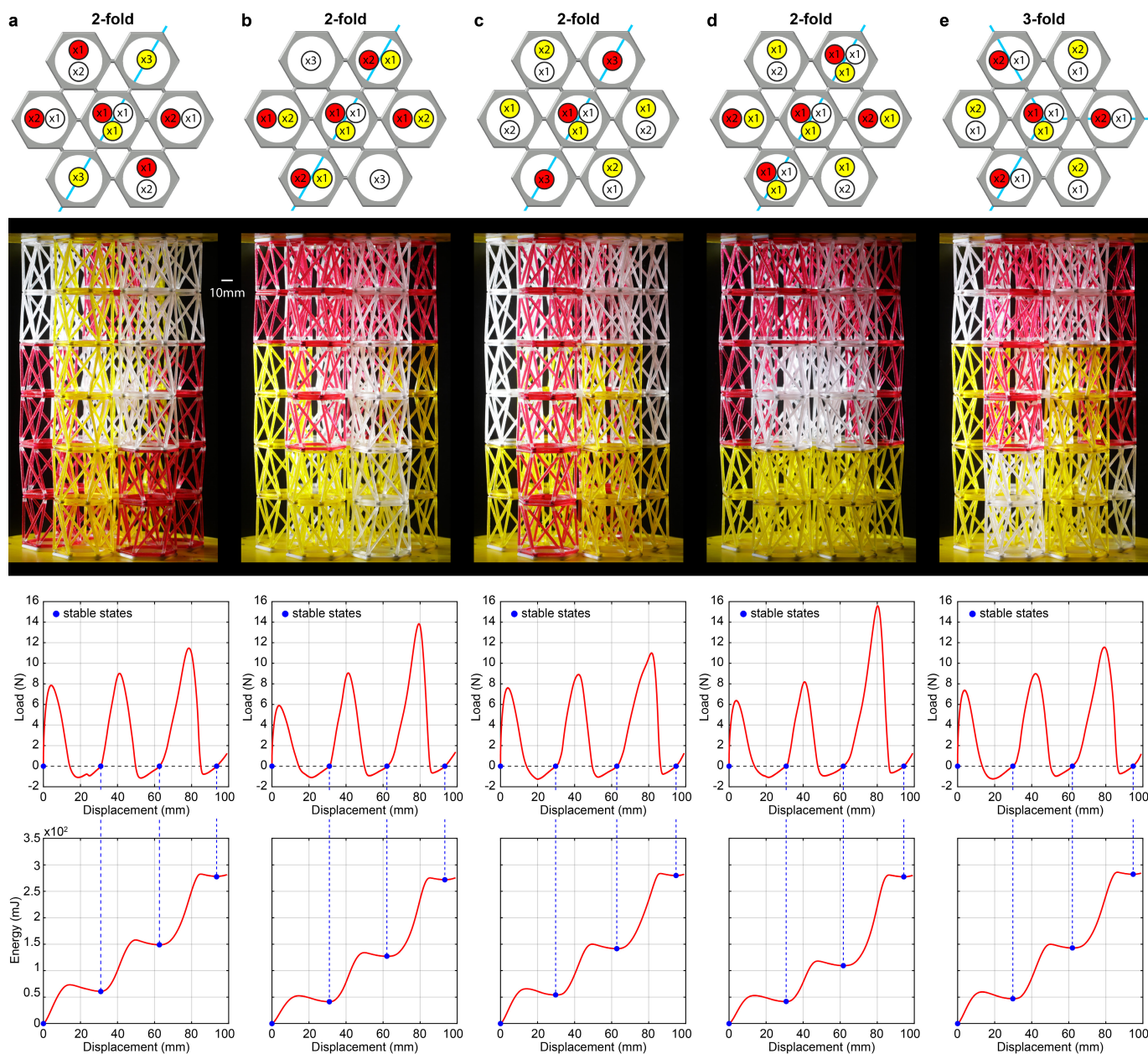


Figure S11: **Alternative reconfigurable assemblies and tunable mechanical responses.** a-e, Five combinations.

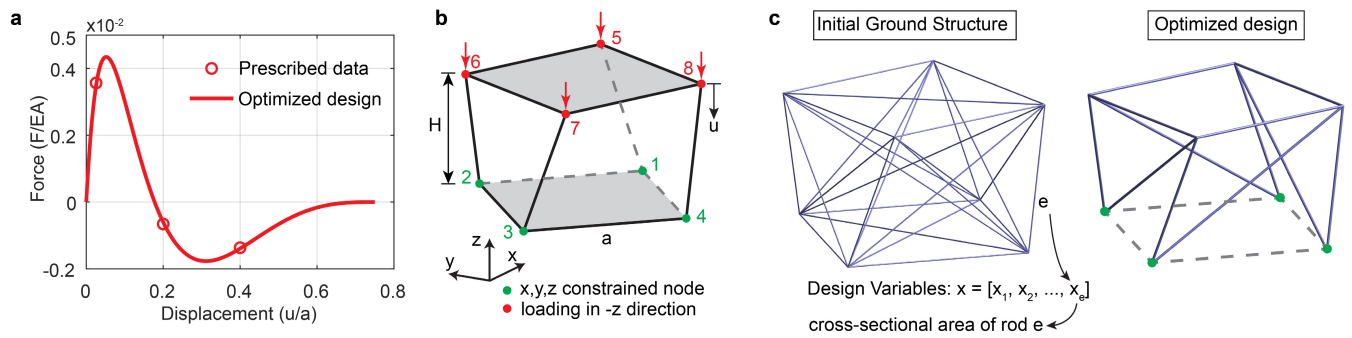


Figure S12: **Inverse-design origami modular cell with desired mechanical properties.** **a**, Prescribed data points on a target force (F/EA)-displacement (u/a) equilibrium trajectory for bistable design. Here A and E denote the cross-sectional area and Young's modulus of the bar elements in the initial ground structure, respectively. **b**, Design domain ($H = 0.75$, $a = 1$), loading, and support conditions. **c**, Layout of the initial ground structure consisting of 28 members (left), and the optimized design (right).

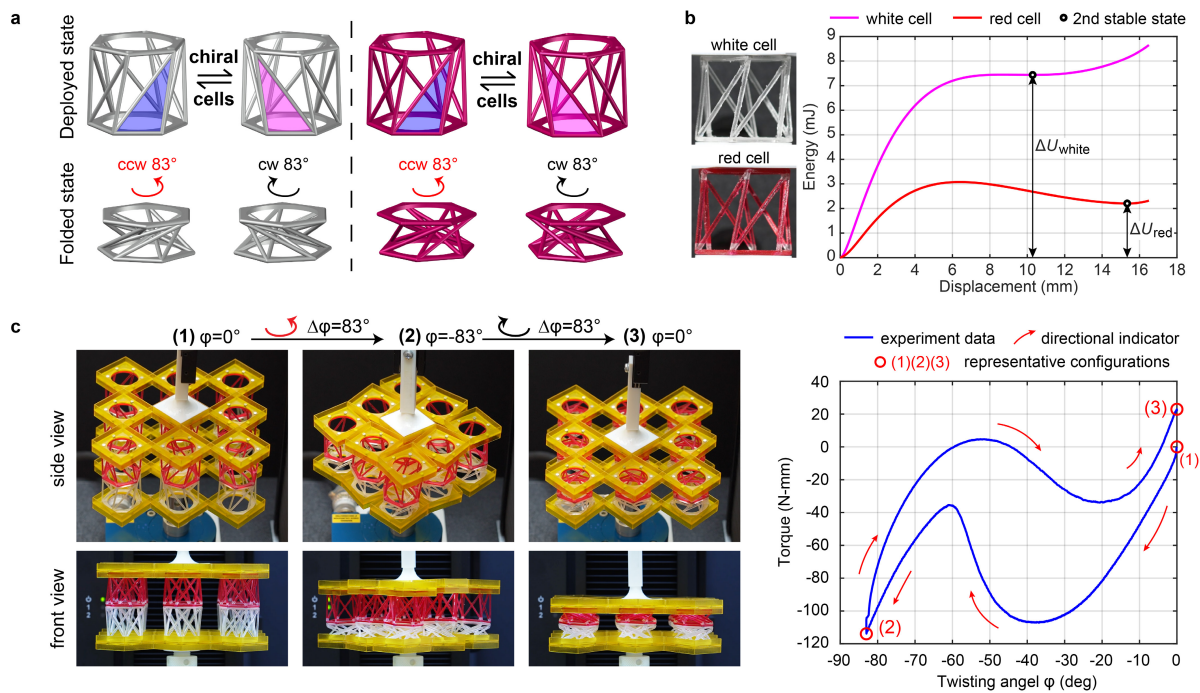


Figure S13: **Twist test for a two-layer assembly composed of chiral cells with distinguishable energy barriers.** **a**, Two sets of chiral unit cells. **b**, Strain energy profile of the two cells. The strain energy is calculated based on the measured force-displacement relationship of the cells. **c**, Left: Three representative states. Right: Measured curve of torque versus twist angle with labels of the three states.

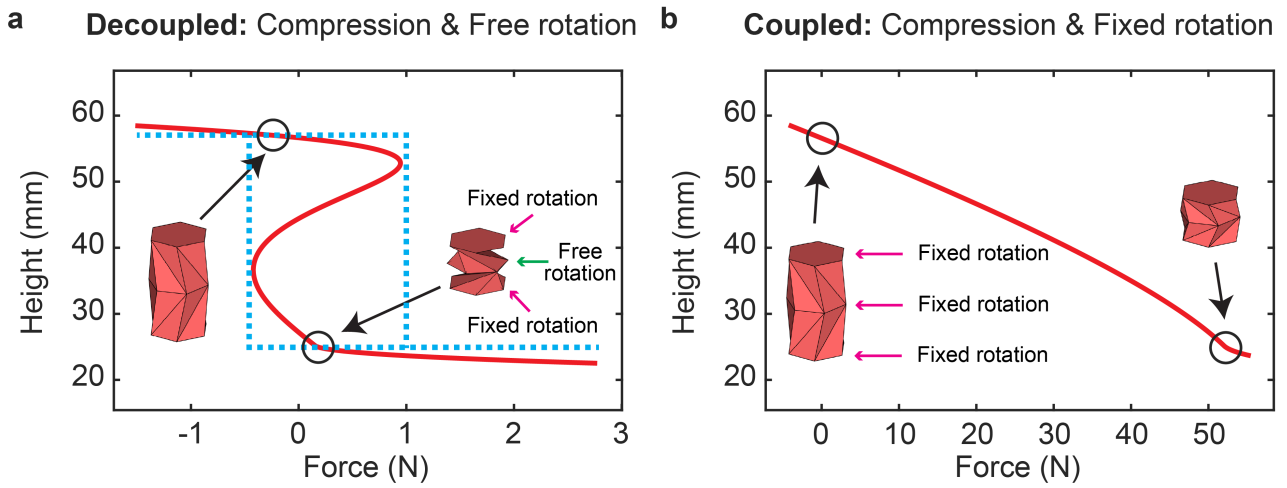


Figure S14: Decoupled and coupled compression responses of the Kresling dipole under displacement (i.e., height) control. **a**, Decoupled simulation. **b**, Coupled simulation.

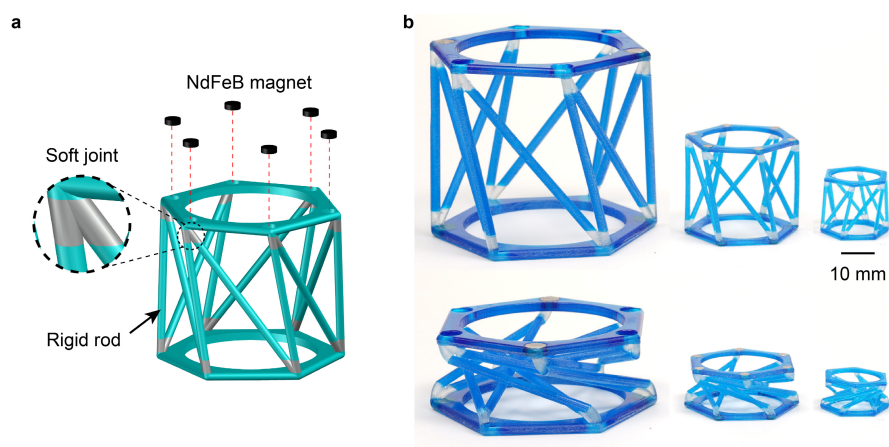


Figure S15: **Modular cell prototyping and scaling.** **a**, CAD modeling of the cell. **b**, Digital images of the cells with three sizes in deployed states (top) and folded states (bottom), respectively.

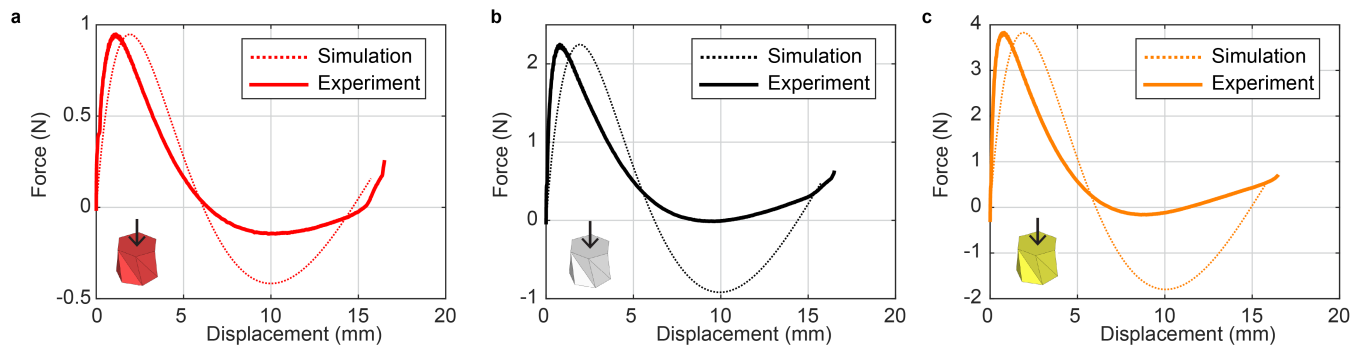


Figure S16: **Compression of three cells of the same geometry but different material properties. a**, The soft material. **b**, The intermediate material. **c**, The hard material. The solid lines represent the average values from three independent tests.

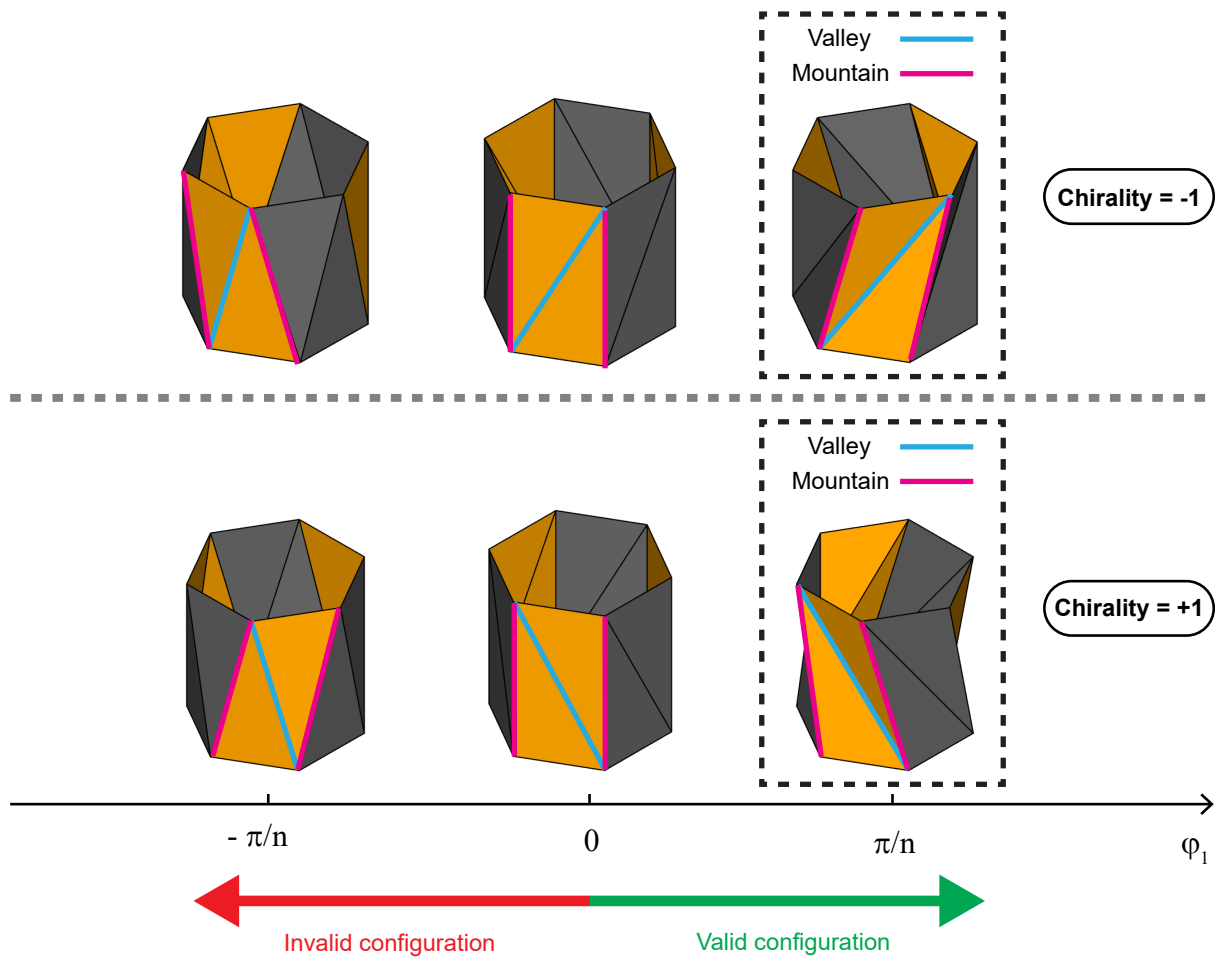


Figure S17: Valid and invalid Kresling origami configurations for different chiralities and initial twist angles. Notice that the horizontal axes do not represent deformations, but different origami configurations.

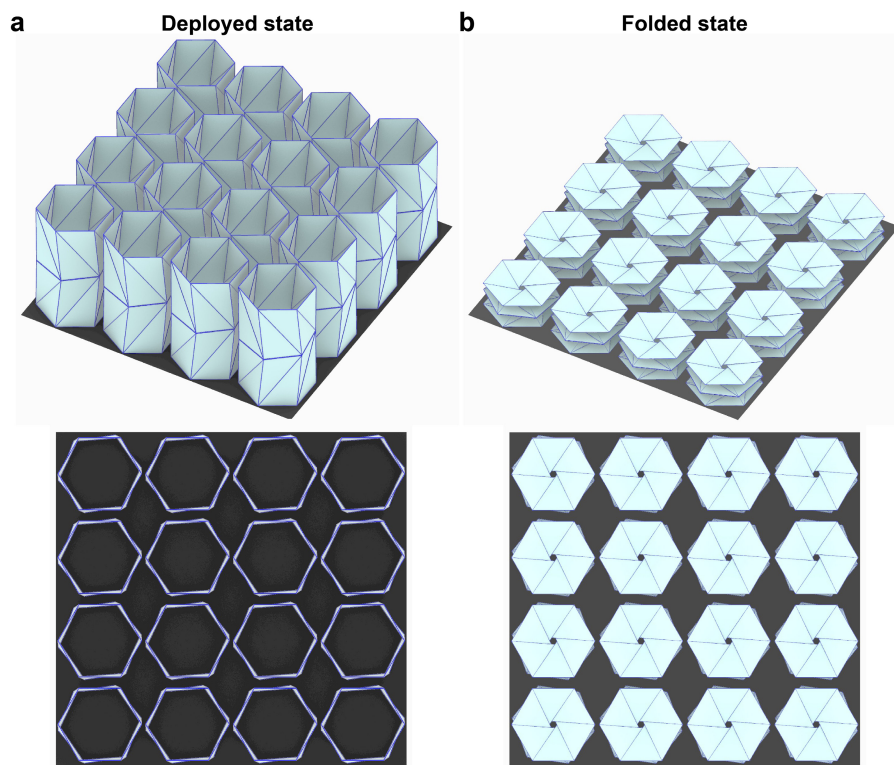


Figure S18: Schematic of thermoregulation with dipole assembly. a, Deployed state. b, Folded state.

References

- [S1] L. Lu, X. Dang, F. Feng, P. Lv, and H. Duan. Conical kresling origami and its applications to curvature and energy programming. *Proceedings of the Royal Society A: Mathematical, Physical and Engineering Sciences*, 478(2257):20210712, 2022.
- [S2] D. Zhao, A. Aili, Y. Zhai, S. Xu, G. Tan, X. Yin, and R. Yang. Radiative sky cooling: Fundamental principles, materials, and applications. *Applied Physics Reviews*, 6(2), 2019.
- [S3] X. Zhao, J. Li, K. Dong, and J. Wu. Switchable and tunable radiative cooling: Mechanisms, applications, and perspectives. *ACS Nano*, 18(28):18118–18128, 2024.
- [S4] G. Chaplin, N. G. Jablonski, R. W. Sussman, and E. A. Kelley. The role of piloerection in primate thermoregulation. *Folia Primatologica*, 85(1):1 – 17, 2013.
- [S5] W. Dorn. Automatic design of optimal structures. *J. de Mecanique*, 3:25–52, 1964.
- [S6] F. Wang, O. Sigmund, and J. S. Jensen. Design of materials with prescribed nonlinear properties. *Journal of the Mechanics and Physics of Solids*, 69:156–174, 2014.
- [S7] E. D. Sanders, A. S. Ramos Jr, and G. H. Paulino. Topology optimization of tension-only cable nets under finite deformations. *Structural and Multidisciplinary Optimization*, 62(2):559–579, 2020.
- [S8] K. Liu and G. H. Paulino. Nonlinear mechanics of non-rigid origami: An efficient computational approach. *Proceedings of the Royal Society A: Mathematical, Physical and Engineering Sciences*, 473(2206):20170348, 2017.
- [S9] S. Wu, T. Zhao, Y. Zhu, and G. H. Paulino. Modular multi-degree-of-freedom soft origami robots with reprogrammable electrothermal actuation. *Proceedings of the National Academy of Sciences*, 121(20):e2322625121, 2024.
- [S10] S. E. Leon, G. H. Paulino, A. Pereira, I. F. M. Menezes, and E. N. Lages. A unified library of nonlinear solution schemes. *Applied Mechanics Reviews*, 64(4):040803, 2011.
- [S11] R. J. Lang. *Twists, Tilings, and Tessellations: Mathematical Methods for Geometric Origami*. CRC Press, Boca Raton, 2017.